Unconventional *s-p-d* hybridization in modulating frontier orbitals of carbonaceous radicals on PdBi nanosheets for efficient ethanol electrooxidation

Liang Ji [a,1], Haiyun Che [b,1], Ningkang Qian [a], Junjie Li [a], Sai Luo [e], Xiao Li [e], Xingqiao Wu [a], Qun Xu [b], Xuzhong Gong [d,*], Xinwei Cui [b,*], Hui Zhang [a,c,**], Deren Yang [a,c]

[a] State Key Laboratory of Silicon Materials and School of Materials Science and Engineering, Zhejiang University, Zhejiang 310027, People's Republic of China
[b] Henan Institute of Advanced Technology, Zhengzhou University, Zhengzhou 450003, People's Republic of China
[c] Zhejiang Provincial Key Laboratory of Power Semiconductor Materials and Devices, ZJU-Hangzhou Global Scientific and Technological Innovation Center, Hangzhou, Zhejiang 311200, People's Republic of China
[d] Institute of Process Engineering, Chinese Academy of Sciences, Beijing 100190, People's Republic of China
[e] Sunrise Power Co., Ltd, Dalian, Liaoning 116024, People's Republic of China

ARTICLE INFO

ABSTRACT

Rational design of highly efficient ethanol electrooxidation catalysts requires modulation of their band structure, yet most of the understanding stops at either upshift or downshift of d-band center that facilitates only a portion of ethanol oxidation reaction (EOR) process. Herein, we take in-situ formed carbonaceous intermediates as an essential part in regulating the band structure of 2D catalysts for the whole EOR process. We found that, by alloying Bi into Pd nanosheets, *d* band of Pd upshifted, resulting in the enhanced adsorption ability of the catalyst. After the adsorption of CH_3CH_2OH, *p* band of Bi dragged down d-band of Pd and lifted up *s* and *p* orbitals of the adsorbed carbonaceous radicals, forming molecular orbitals that bridged their energy gaps and lowered the energy barriers of electron transfer in C1 pathway. This unconventional *s-p-d* hybridization offers $Pd_{14.9}Bi$ nanosheets exhibit high mass activity of 6.6 A/mg_{pd} and C1 selectivity of 19.7 %.

1. Introduction

Direct ethanol fuel cells (DEFCs) are among the most promising energy conversion devices owing to their high theoretical energy density (8 kWh kg^{-1}), low toxicity, and easy accessibility from biomass [1–3]. The bottleneck, however, is the inadequate activity for ethanol oxidation reaction (EOR) at the anode of DEFCs. This unsatisfied activity is originated from incomplete oxidation of ethanol with only 4 electrons transfer (C2 pathway), resulting in the formation of acetic acid or acetate as the final products [4–6]. C1 pathway, on the other hand, is highly preferred because of the ethanol oxidation all the way to CO_2 or carbonate with 12 electrons transfer [7,8]. Nonetheless, it is severely hampered by high energy barrier of C—C bond cleavage as well as the sluggish oxidation of various carbonaceous intermediates such as *CH$_x$

and *CO$_{ad}$ [9–12]. Hence, rational construction of the electrocatalysts with the tunable band structure is highly desired since it can promote the reaction kinetics of all the oxidation steps in C1 pathway and improve the C1 selectivity.

C1 pathway starts from the adsorption of CH_3CH_2OH and its sequential oxidation to *CH_3CO, *CH_3 + *CO, 2 * CO, 2 * CO_2, and then the desorption of CO_2 [13–15]. All these steps are highly connected and interactive, yet give contradictory requirements on the shift of d-band center. For example, Yang et al. found that the surface tension of the Ag@PdP catalysts leaded to the upshift of d-band center, and thus strengthened the adsorption ability of reactive species. This feature could promote the formation of *CH_3CO and *OH_{ad}, and thus improve the catalytic properties for EOR [16]. In another study, Shen et al. demonstrated that the downshift of d-band center in PdCoH nanosheets

---

could weaken the adsorption of CO, leading to the improved C1 pathway selectivity and anti-poisoning ability [17]. According to the d-band center theory, it is generally recognized that the upshift of the d-band center increases the electron density around Fermi level, which facilitates the adsorption of CH_3CH_2OH and the carbonaceous intermediates [18,19]. However, the strengthened adsorption of CO also results in the poisoning of the catalyst [20]. On the contrary, the downshift of the d-band center weakens the affinity of the adsorbed species, which effectively alleviates the toxic intermediate but fails in facilitating the oxidation process of carbonaceous radicals thus deteriorates the activity [21]. Therefore, the contradictive requirements on the position of d-band center makes the kinetics of carbonaceous radical adsorption, the toxic intermediate elimination, and the electron transfer in C1 pathway almost impossible to improve simultaneously. Such contradiction poses a tremendous challenge in design and construction of highly efficient EOR catalysts.

Up to now, Pt- and Pd-based electrocatalysts have been widely studied for EOR but still with unsatisfied activity [22,23], where Pd is much more abundant than Pt in the earth curst and exhibits superior dehydrogenation performance in alkaline media [12]. Introducing oxophilic metals (such as Co, Ni, Zn, etc.) in Pt or Pd can on one hand facilitate the formation of OH radicals, and thus improve the oxidation process of carbonaceous intermediates [17,24–27]. On the other hand, d-band center of Pt or Pd can be modulated by the formation of alloys with a second metal, which is crucial for adsorption of reaction intermediates [28]. Nevertheless, to comprehensively understand the EOR process, the coherent shift of all the frontier bands in the alloyed catalysts should be analyzed separately rather than the average shift of the d-band center. More importantly, we propose that the frontier orbitals of carbonaceous radicals also render us with a powerful tool in regulating the band structure of the catalysts during the progress of EOR. However, the orbitals of the adsorbed species only affect several atoms in distance along the thickness direction [29], raising special requisites on the dimensions of the desired catalyst.

Herein, 2D ultrathin PdBi nanosheet (NS) catalysts have been selected and fabricated through a facile and one-pot solvothermal method. The obtained ultrathin 2D porous nanosheet with the optimal composition of $Pd_{14.9}Bi$ presented a high mass activity of 6.6 A/mg_{pd} and a high specific activity of 17.9 mA/cm^2, with the selectivity of C1 pathway reaching as high as 19.7 %. Density functional theory (DFT) calculations elucidated that the unconventional *s-p-d* hybridization has been successfully established among *s* and *p* orbitals of the adsorbed carbonaceous radicals, *p* band of Bi, and *d* band of Pd, well explaining the promoted kinetics of all the oxidation steps in C1 pathway and the synergistic improvement of both activity and anti-poisoning ability. Our findings deepen the understanding on the relationship between the band structure modulation and EOR activity, and also provide a useful guidance in designing highly efficient catalysts for a broad range of electrocatalysis.

2. Experimental section

2.1. Materials and chemicals

Sodium tetrachloropalladate (Na_2PdCl_4), bismuth triacetate ($C_6H_9BiO_6$), tungsten carbonyl ($W(CO)_6$) were purchased from Sigma Aldrich. N,N-Dimethylformamide (DMF), acetic acid (CH_3COOH) and ethanol were purchased from Sinopharm Chemical Reagent Co., Ltd. (China). The deionized water (DI water) with resistivity of 18.2 MΩ/cm was obtained by ultrapure water system. All the reagents mentioned above were used without further purification.

2.2. Preparations of PdBi nanosheets with different molar ratios

In a typical synthesis procedure of $Pd_{14.9}Bi$ NS, 10 mg of Na_2PdCl_4, 1 mg of $C_6H_9BiO_6$ and 25 mg of $W(CO)_6$ were added into a 20 mL glass vial

with 8 mL of DMF and 2 mL of acetic acid. After carefully capped, the vial was transferred to a magnetic stirrer stirring for 30 min to form a transparent solution. Next, the vial was transferred into an oil bath maintaining at 140 °C for 1 h. Finally, the powder products can be obtained after washed with ethanol and freezing dried. The synthesis procedures of Pd, $Pd_{28.5}Bi$, $Pd_{8.7}Bi$ and $Pd_{4.5}Bi$ NSs were similar to that of $Pd_{14.9}Bi$ NS, except that the usage of $C_6H_9BiO_6$ is 0, 0.5, 2 and 4 mg, respectively.

2.3. Characterizations

The morphology of the samples were obtained through filed-emission scanning electron microscopy (SEM,Hitachi S-4800) and transmission electron microscopy (TEM, Hitachi HT-7700) operated at 100 kV. High-resolution transmission electron microscopy (HRTEM, FEI Tecnai F20 G2) was operated at 200 kV. The aberration-corrected high-angle annular dark-filed (HAADF) STEM images was taken on FEI Titan ChemiSTEM. The X-ray diffraction patterns (XRD) was characterized by Bruker D8 with copper Kα radiation. X-ray photoelectron spectrometer (XPS) was carried out on Axis Supra (Kratos Inc) with Al Kα radiation. Inductively coupled plasma atomic emission spectrometry (ICP-AES) was taken on IRIS Intrepid II XSP (TJA Co., USA).

2.4. Electrochemical measurements

An electrochemical workstation (CHI760E, Shanghai Chenhua Co., Ltd) with a standard three-electrode cell system was carried out to achieve all the electrochemical measurements. A glassy carbon electrode with the surface area of 0.196 cm^2 was used as working electrode, the loading weight of Pd on which is 2 μg. A platinum wire and a standard calomel electrode (SCE) was used as counter and reference electrode respectively. The ethanol oxidation reaction was performed in solution containing 0.5 M KOH and 1 M ethanol. The electrochemical active surface area (ECSA) was analyzed via CO stripping measurement. Briefly, the cyclic voltammetry (CV) curves of different samples were conducted at room temperature in CO-saturated and Ar-saturated solution containing 1 M ethanol and 0.5 M KOH respectively. The sweeping rate is 50 mV/s between 0 and 1 V (RHE). The ECSA of different catalysts were calculated through the following equation:

$$ECSA = \frac{Q_{CO}}{0.42mC \cdot cm^{-2} \times m_{Pd}}$$

where Q_{CO} stands for the charge which can be calculated through integrating the oxidation peak area, m_{Pd} is the mass loading on RDE and 0.42 mC cm^{-2} is charge required for the oxidation of CO.

2.5. Electrochemical in-situ FTIR analysis

The FTIR spectra of EOR process was collected on Bruker vertex 70 V equipped with a liquid nitrogen-cooled MCT-A detector by internal reflection method. The catalyst was dropped on silicon crystal coated with a thin Au film, which was used as working electrode. A platinum wire and a standard calomel electrode (SCE) was used as counter and reference electrode respectively. The EOR process was conducted in 0.5 M KOH and 1 M ethanol solution in a homemade cell. Before each test, the electrode was held at 0.35 V (SCE) to clean the surface of the catalyst, then different potential was applied to collect the spectrum. All of the spectrums were collected with 128 interferograms and a resolution of 8 cm^{-1}.

2.6. Calculation of C1 selectivity

The Faraday efficiency (FE) of possible C1 product were obtained by HPLC ((Beijing Liyuan, EP-1000D). The catalyst was first drop casted on a 1 cm × 1 cm carbon paper electrode with the mass loading of 1 mg.

Then chronoamperometric tests were carried out in 60 mL electrolyte containing 0.5 M KOH and 1 M ethanol with the catalyst to accumulate 30 C electrons at different potentials. The concentrations of acetic acid and acetaldehyde in the electrolyte after the test were collected and quantitatively measured by HPLC through the integrating of the peak area, where acetaldehyde was derived by 2,4-dinitrophenylhydrazone (DNPH). A series of standard solutions (1, 5, 10 ppm of acetic acid and acetaldehyde) were measured and the concentration standard curves can be obtained in HPLC. Finally, the Faradic efficiency of the C2 products can be obtained by using the follow equation:

$$FE_{C2} = \frac{n \times N \times F}{Q} \times 100\%$$

where n is the moles of the product measured by HPLC, N is the number of electron transfer, F is the Faraday constant (96,485 C/mol), and Q is the total charge obtained by the electrochemical workstation. Finally, the possible FE of C1 product can be obtained by $1 - FE_{C2}$.

2.7. DFT calculations

Vienna Ab Initio Simulation Package (VASP) was applied to conduct the first-principles calculations [30,31], using a generalized gradient approximation (GGA) of exchange-correlation functional in the Perdew, Burke, and Ernzerhof (PBE). van der Waals corrections were also considered by using the DFT-D3 method of Grimme [32–34]. A plane-wave energy cut off of 400 eV was used together with norm-conserving pseudopotentials, and Γ-centered $6 \times 6 \times 1$ k-point was applied correspondingly. An energy of 1×10^{-6} eV and a force of 0.01 eV/Å^{-1} were set for geometry optimizations. The unitcells of Pd and PdBi (PdBi = 15:1) were first optimized, and then a $4 \times 4 \times 1$
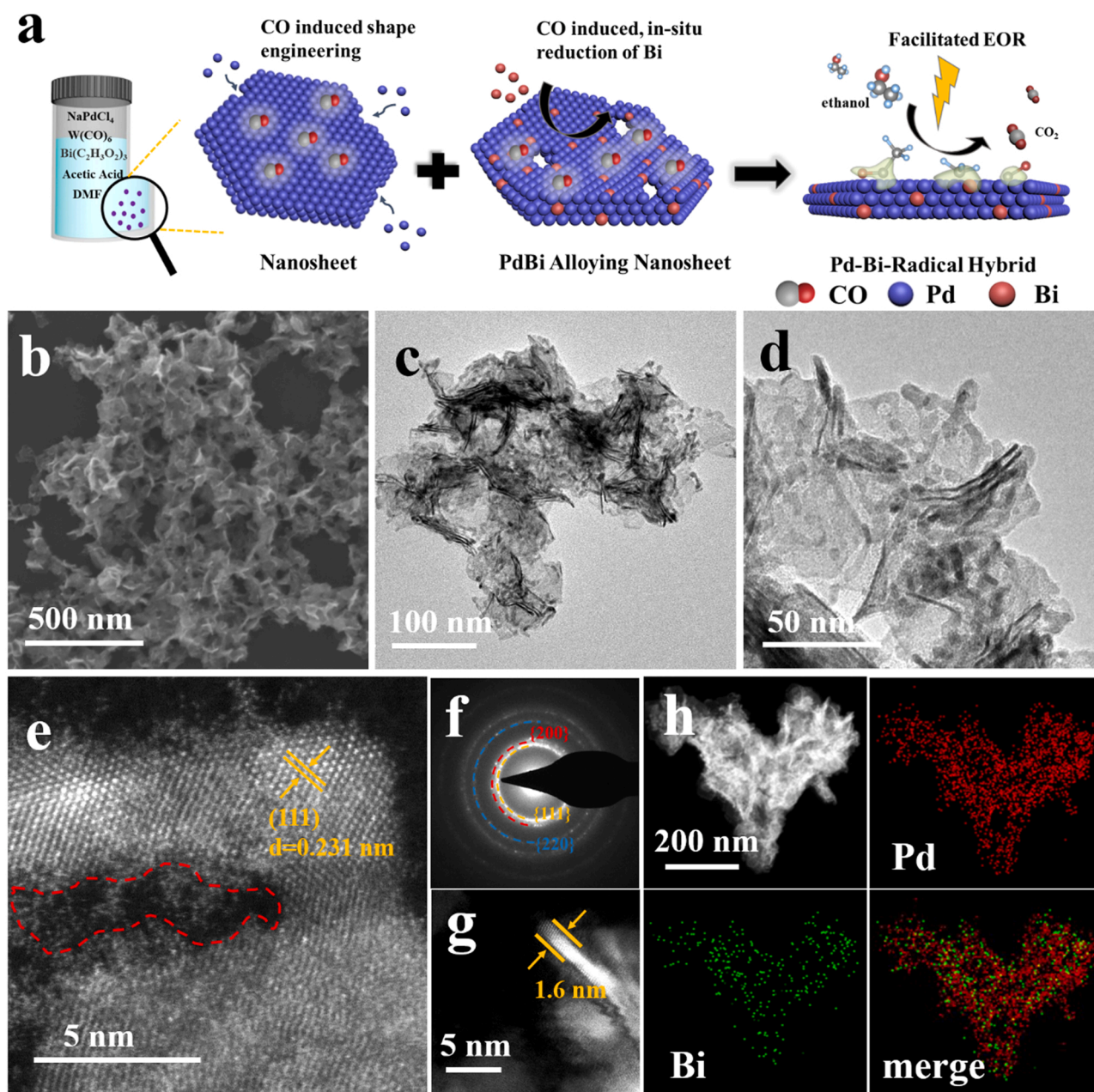

Fig. 1. Morphology and structural characterization of PdBi NS. (a) Schematic illustration of the formation process of PdBi NS. (b) SEM image of Pd$_{14.9}$Bi NS. (c, d) TEM images of Pd$_{14.9}$Bi NS. (e) HAADF-STEM image of the surface of Pd$_{14.9}$Bi NS, the area marked by a dashed red circle represents the porous structure. (f) SAED pattern of Pd$_{14.9}$Bi NS. (g) The cross-section HAADF image of Pd$_{14.9}$Bi NS, showing the thickness of 7 atomic layer. (h) EDX mapping images of Pd$_{14.9}$Bi NS.

supercells were constructed. According to TEM observations, the surface cleavage was conducted for the exposure of (110) to accommodate the adsorption of cabonaceous radicals, based on which electronic properties were calculated. To eliminate artificial interactions induced by the periodic boundary condition, a vacuum region of 15 Å was added in the slab model. The thickness of the slab was set to be 5 at. layers, where the bottoms two layers were fixed. The free energy (*G*) was computed from $G = E + ZPE - T\Delta S$, where *E* was the total energy, *ZPE* was the zero-point energy, the entropy (ΔS) of each adsorbed state were yielded from DFT calculations, whereas the thermodynamic corrections for gas molecules were from standard tables.

3. Results and discussion

3.1. Characterization of ultrathin PdBi NS catalysts

Ultrathin PdBi NS catalysts were synthesized via a facile, one-pot solvothermal strategy as illustrated in Fig. 1a. In a typical example, $Pd_{14.9}Bi$ NS was fabricated by adding 10 mg of Na_2PdCl_4, 1 mg of $C_6H_9BiO_6$ and 25 mg of $W(CO)_6$ into a glass vial with 8 mL of DMF and 2 mL of acetic acid, where Na_2PdCl_4 and $C_6H_9BiO_6$ were used as the precursors for Pd and Bi, respectively, $W(CO)_6$ and DMF as the reducing agents. It is noted that Na_2PdCl_4 can combine with CO and acetic acid to form the $Pd_4(CO)_4(CH_3COO)_4$ complex during the synthetic process [35]. This complex can decompose to atomic Pd clusters and continually adsorb onto the edges of the existing atomic Pd clusters. CO molecules released by $W(CO)_6$ can also be easily adsorbed but prevent the growth of Pd clusters. It is suggested that the competitive adsorptions between $Pd_4(CO)_4(CH_3COO)_4$ complex and CO on various surfaces result in an anisotropic growth, assisting the preferential formation of ultrathin alloyed nanosheets [35–37]. In addition, the in-situ formed CO can also act as a strong reducing agent for the simultaneous deposition of Pd and Bi so as to form the desired PdBi NS. The synthetic mechanism and a series of PdBi NS catalysts have been presented in the Supporting information (Figs. S1–S4).

The analyses of morphology and microstructure of $Pd_{14.9}Bi$ NS were performed, as shown in Fig. 1. Scanning electron microscopy (SEM) image in Fig. 1b shows the uniform distribution of three-dimensional wrinkled structures, which are comprised of many ultrathin nanosheets (Fig. 1c). Transmission electron microscopy (TEM) images in Fig. 1c and Fig. 1d show that the nanosheets are similar in size with the lateral size at around 60 nm. High-angle annular dark-field scanning electron microscopy (HAADF-STEM) in Fig. 1e and the diffraction pattern in Fig. 1f demonstrate that the nanosheets maintain face-centered cubic (fcc) crystal structure as that of pure Pd. However, the lattice spacing of (111) measured in Fig. 1e shows a D-spacing of 0.231 nm, which is a little larger than that of pure Pd (0.227 nm), suggesting the formation of PdBi alloy phase. In addition, nanometer-size pores are also present in the nanosheet, labelled as the dashed red circle in Fig. 1e, which is beneficial for the exposure of a large amount of active sites for ethanol electrooxidation [38]. More importantly, the cross section of the nanosheets in Fig. 1g shows a thickness of ~ 1.6 nm with 7 atomic layers, confirming the successful formation of PdBi NS. Energy dispersive X-ray spectroscopy (EDX) mapping images in Fig. 1h further illustrates the uniform distribution of Pd and Bi with the atomic ratio of Pd/Bi being 93.4:6.6, which is close to the result (93.7:6.3) obtained by inductively coupled plasma atomic emission spectroscopy (ICP-AES). Taken together, the obtained nanosheets are $Pd_{14.9}Bi$ alloyed NS.

X-ray diffraction (XRD) patterns in Fig. 2a shows the negative shift of (111) plane from 39.3° for Pd NS to 39° for $Pd_{14.9}Bi$ NS, confirming the alloyed nature of the obtained structure, which is consistent with HAADF image and EDX mapping results in Fig. 1. X-ray photoelectron spectroscopy (XPS) was conducted to analyze the chemical state and electron interaction between Pd and Bi in $Pd_{14.9}Bi$ NS. It can be found that Pd and Bi are mainly in their metallic states (Fig. S5). In addition, Pd $3d_{3/2}$ and Pd $3d_{5/2}$ peaks in Fig. 2b shift negatively about 0.55 eV in $Pd_{14.9}Bi$ NS in comparison with those in Pd NS, suggesting the electron
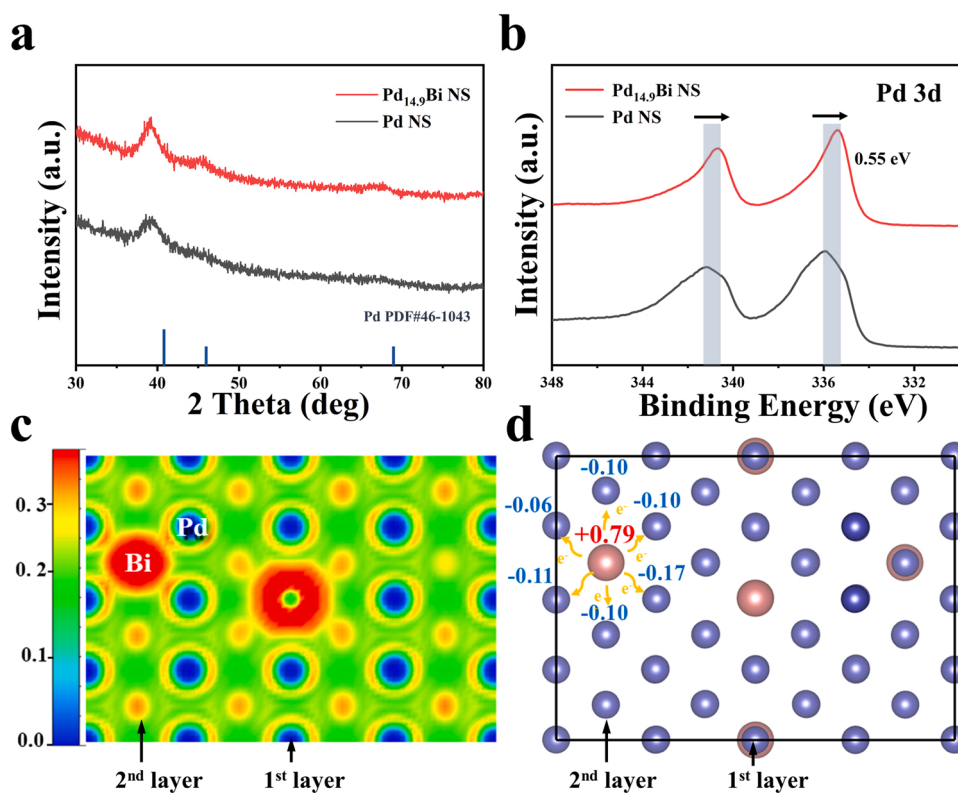

Fig. 2. Phase and electronic structures of $Pd_{14.9}Bi$ NS and Pd NS. (a) XRD patterns of $Pd_{14.9}Bi$ NS and Pd NS. (b) XPS spectra of Pd 3d taken from $Pd_{14.9}Bi$ NS and Pd NS. (c) The electron localization function analysis mapped for PdBi NS. (d) Bader charge analysis of PdBi NS, illustrating the electron transfer from Bi to Pd.

transfer from Bi atoms to Pd atoms. In order to understand the electronic structure of $Pd_{14.9}Bi$ NS, we conducted DFT calculations. The optimized structures of Pd NS and PdBi NS (PdBi = 15:1) can be seen in Fig. S6 with the expansion of the supercell along *a* and *b* axes due to the alloying of Bi atoms. The electron localization function analysis in Fig. 2c and Fig. S7 reveals that the electrons are more localized along Pd-Bi bonds, suggesting the existence of electron transfer between Bi and Pd. The electron transfer from Bi to its surrounding Pd atoms was proved by the Bader charge analysis in Fig. 2d (Bi atoms present an average charge of + 0.79 e), which is consistent with XPS observations, and thus enriches the surface electron density of Pd atoms.

3.2. Application of PdBi NS catalysts for EOR

Electrochemical EOR tests were then performed for commercial Pd/C, Pd NS, and a series of PdBi NS in Ar-saturated 0.5 M KOH + 1 M ethanol solution (Fig. 3). Fig. 3a–c demonstrate the prominent enhancement in EOR activity for $Pd_{14.9}Bi$ NS in comparison with Pd/C and Pd NS. The EOR mass activity of $Pd_{14.9}Bi$ NS can be determined from mass-normalized CV curves in Fig. 3a, which was calculated to be 6.60 A/mg_{pd}. It is 6.3 and 2.0 times higher than those of Pd/C (1.05 A/mg_{pd}) and Pd NS (3.29 A/mg_{pd}), respectively. This improvement can be ascribed to the synergistic effect of incorporation of Bi and enhancement in electrochemical active surface area (ECSA). As shown in Fig. S8 and Table S1, $Pd_{14.9}Bi$ NS possesses the highest ECSA value among all the tested samples, suggesting the exposure of the largest active surface area for EOR and thus the enhanced mass activity. The increased ECSA should be correlated with the 2D ultrathin porous sheet-like structure of the alloyed nanosheet. Interestingly, the ECSA-normalized CV curves in Fig. 3b also give the best specific activity of 17.90 mA/cm^2 for $Pd_{14.9}Bi$ NS, which is 4.7 and 1.56 times higher than those of Pd/C (3.80 mA/cm^2) and Pd NS (11.53 mA/cm^2), respectively. The performance also demonstrates to be outstanding among state-of-the-art catalysts in Table S2. This result suggests that the reactive sites in the alloyed nanosheet are more active for EOR than those on Pd/C and Pd NS, which should be attributed to the particular electronic structure after the alloying of Bi atoms into the 2D Pd matrix. Fig. 3d shows the smallest

diameter in electrochemical impedance spectroscopy (EIS) measurements and Fig. 3e shows the smallest current decay in the chronoamperometry test carried out at the potential of 0.8 V (vs. RHE) for 3600 s. Meanwhile, after 1000 cycles in CV tests, PdBi NS retains the largest mass activity as shown in Fig. S9, which also demonstrates the superior EOR kinetics and stability performance for $Pd_{14.9}Bi$ NS. After the durability test, Pd NS has been broken into nanoparticles as shown in Fig. S10a, while most PdBi NSs maintain their original sheet-like structure (Fig. S10b and c). XPS analyses of the catalysts after the durability test (Fig. S10d–f) show that the oxidation of Pd is much less pronounced for $Pd14.9Bi$ NS (Fig. S10e) than that for Pd NS (Fig. S10d). Since the chemical state of Bi in Fig. S10f also keeps similar to their initial state (Fig. S5c), it is suggested that Bi can stabilize the nearby Pd atoms for the improved long-term stability compared with Pd NS and Pd/C. Furthermore, when comparing the EOR performance of the alloyed NS with different atomic ratios of Pd/Bi, $Pd_{14.9}Bi$ NS still holds the best one (Fig. 3f and Fig. S11), which may be due to the combined effects of ECSA exposed from the 2D porous structure (Fig. S3) and the activity originated from the electronic structure at that specific composition.

As discussed in Fig. 2, electron transfer from Bi to Pd increases surface electron density of Pd atoms in PdBi NS, which can facilitate the adsorption of CH_3CH_2OH and promote C—C bond cleavage, leading to the improvement of EOR activity [39]. However, the increased adsorption capability normally impairs the ability to eliminate the toxic intermediate of CO, resulting in the poisoning of the catalysts. Hence, it is essential to evaluate the anti-poisoning property of our catalysts. It is known that the ratio of forward peak current (I_f) to backward peak current (I_b) in Fig. 3a is an important indicator of the anti-poisoning ability [40,41]. Interestingly, the $Pd_{14.9}Bi$ NS in this work shows a high I_f/I_b value of 1.68, almost double that for Pd/C (0.91) and that for Pd NS (0.93). The improved anti-poisoning ability was also proved by CO-stripping test in Fig. S8, where the $Pd_{14.9}Bi$ NS gives the most negative onset potential.

The simultaneous achievement of high EOR activity and anti-poisoning capability encourages us to investigate the C1 selectivity and the energy barrier changes for C1 and C2 pathways further. In
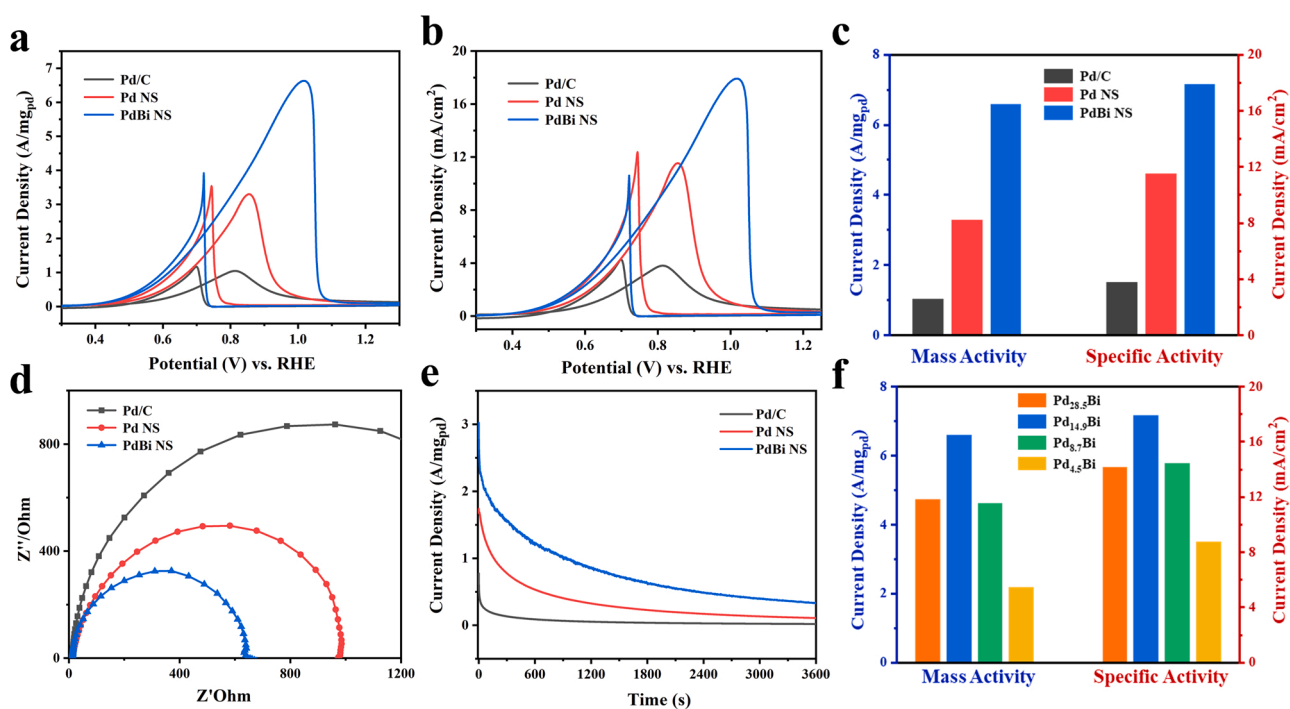

Fig. 3. Electrochemical performance toward EOR. (a) Mass-normalized and (b) ECSA-normalized EOR CV curves. (c) Mass and specific activities of Pd/C, Pd NS and $Pd_{14.9}Bi$ NS. (d) Nyquist plots of these catalysts. (e) i-t curves of these catalysts at 0.8 V. (f) Mass and specific activities of PdBi NS with different compositions.

determining the C1 selectivity, in-situ FTIR spectroscopy measurement has been performed. As illustrated in Fig. 4a–c, the upward bands locating at 1045 and 1085 cm^{-1} are related with C-O stretching vibration of the consumed ethanol [42,43]. Two downward peaks at 1412 and 1551 cm^{-1} can be assigned to symmetrical and asymmetric stretching vibrational modes of O-C-O in acetate ions (CH$_3$CHO$^-$), which indicates the formation of C2 products [44,45]. In particular, the O-C-O asymmetric stretching of CO$_2$ is located at 2340 cm^{-1} [12,46], which implies the final product of C1 pathway. It is clear that the CO$_2$ band is much stronger for Pd$_{14.9}$Bi NS (Fig. 4c) than those for Pd/C (Fig. 4a) and Pd NS (Fig. 4b), indicating the significantly enhanced CO$_2$ productivity. Moreover, the band at 1412 cm^{-1} of Pd$_{14.9}$Bi NS is as strong as that at 1551 cm^{-1}, which can be ascribed to the overlap of the in-situ formed CO$_3^{2-}$ from C1 with CH$_3$COO$^-$ from C2 near 1412 cm^{-1} [17], also strongly demonstrating the improved selectivity of C1 pathway. To quantify the selectivity between C1 and C2 pathways, the electrolytes after chronoamperometric tests were collected and analyzed by HPLC with the standard curves shown in Fig. S12. The calculated results in Fig. 4d shows that Pd$_{14.9}$Bi NS presents the highest C1 selectivity at 1.0 V with the Faradic efficiency (FE) of 19.7 %, which is superior to those of

commercial Pd/C (3.3 %) and Pd NS (5.9 %). In addition, the FE values at various potentials for Pd$_{14.9}$Bi NS were also provided in Fig. S13.

The free energy diagrams of C1 and C2 pathways were also calculated by DFT for the energetic view of the EOR process. It is clear in Fig. 4e that the electrochemical rate-determining step for C1 pathway is the oxidation of [*CH$_3$→*CO], which is consistent with previous reports [47]. The energy barrier of this oxidation step decreases from 1.50 eV for Pd NS to 1.18 eV for Pd$_{14.9}$Bi NS. At the same time, the energy barrier of C2 pathway increases significantly from 0.72 eV for Pd NS to 2.92 eV for Pd$_{14.9}$Bi NS. As *CH$_3$CO is the common intermediate in both pathways, the lower energy barriers of C-C bond cleavage (Fig. S14) and the subsequent oxidation steps in C1 pathway, as well as the higher activation barriers in C2 pathway, demonstrate that the selectivity of C1 pathway is significantly boosted after the incorporation of Bi. In addition, the energy barrier for the oxidation of [*CO→CO$_2$] has also been reduced, as shown in Fig. 4e, facilitating the kinetics of eliminating CO and preventing the poisoning of the alloyed nanosheet. All these energy changes in the reaction pathways explicate much enhanced C1 selectivity, EOR activity, and anti-poisoning capability observed in the experimental results for Pd$_{14.9}$Bi NS.

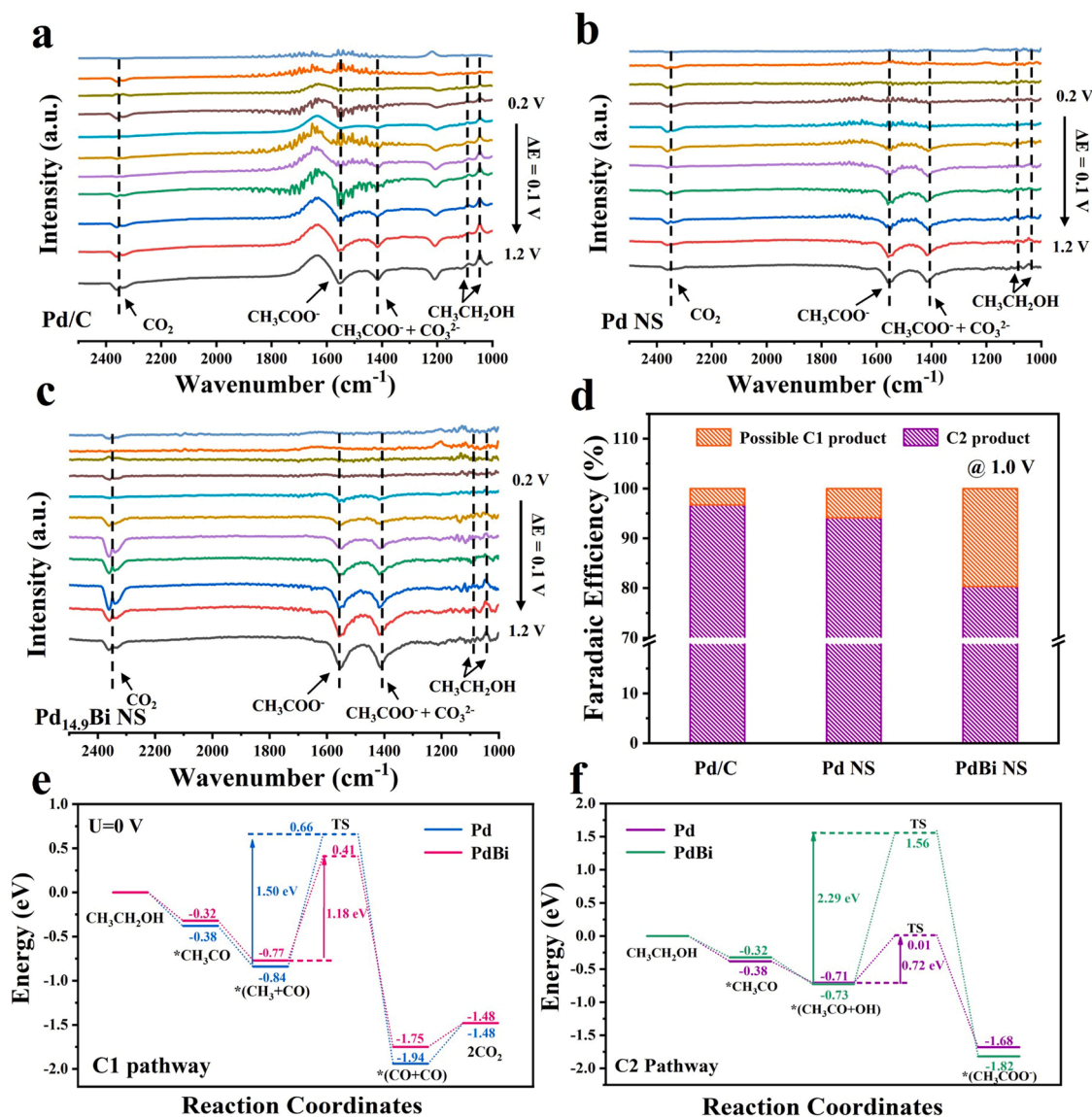**Fig. 4.** In situ FTIR spectrum and free energy diagram. In situ FTIR spectra of (a) Pd/C, (b) Pd NS and (c) Pd$_{14.9}$Bi NS at different potentials from 0.2 to 1.2 V (RHE) in 0.5 M KOH + 1 M ethanol solution. (d) Faradaic efficiencies of Pd/C, Pd NS and Pd$_{14.9}$Bi NS with C1 and C2 products at 1.0 V. (e) Free energy diagram of C1 reaction pathway on Pd NS and PdBi NS. (f) Free energy diagram of C2 reaction pathway on Pd NS and PdBi NS.

3.3. Insights into how s-p-d hybridization improved the EOR performance

In order to gain fundamental insights into the energy changes in C1 pathway in Fig. 4e, we analyzed the changes of the band structure arising from the alloyed Bi, and more importantly, the adsorbed carbonaceous radicals during the progress of EOR starting from the adsorption step. The calculations of partial density of states (PDOS) were

carried out by DFT. It is demonstrated in Fig. 5a that the electron states shift up and a little over the Fermi level (indicated by the black arrow in Fig. 5a) because of the electron transfer from Bi to Pd, enriching the surface electron density of Pd atoms for the improved adsorption capability of CH_3CH_2OH (Fig. S15). In addition, Fig. 5b shows that d and s orbitals of Bi atoms are far away from d band of Pd, while p orbital of Bi atoms hydrides with d band of Pd in the PdBi NS (as shown by red lines
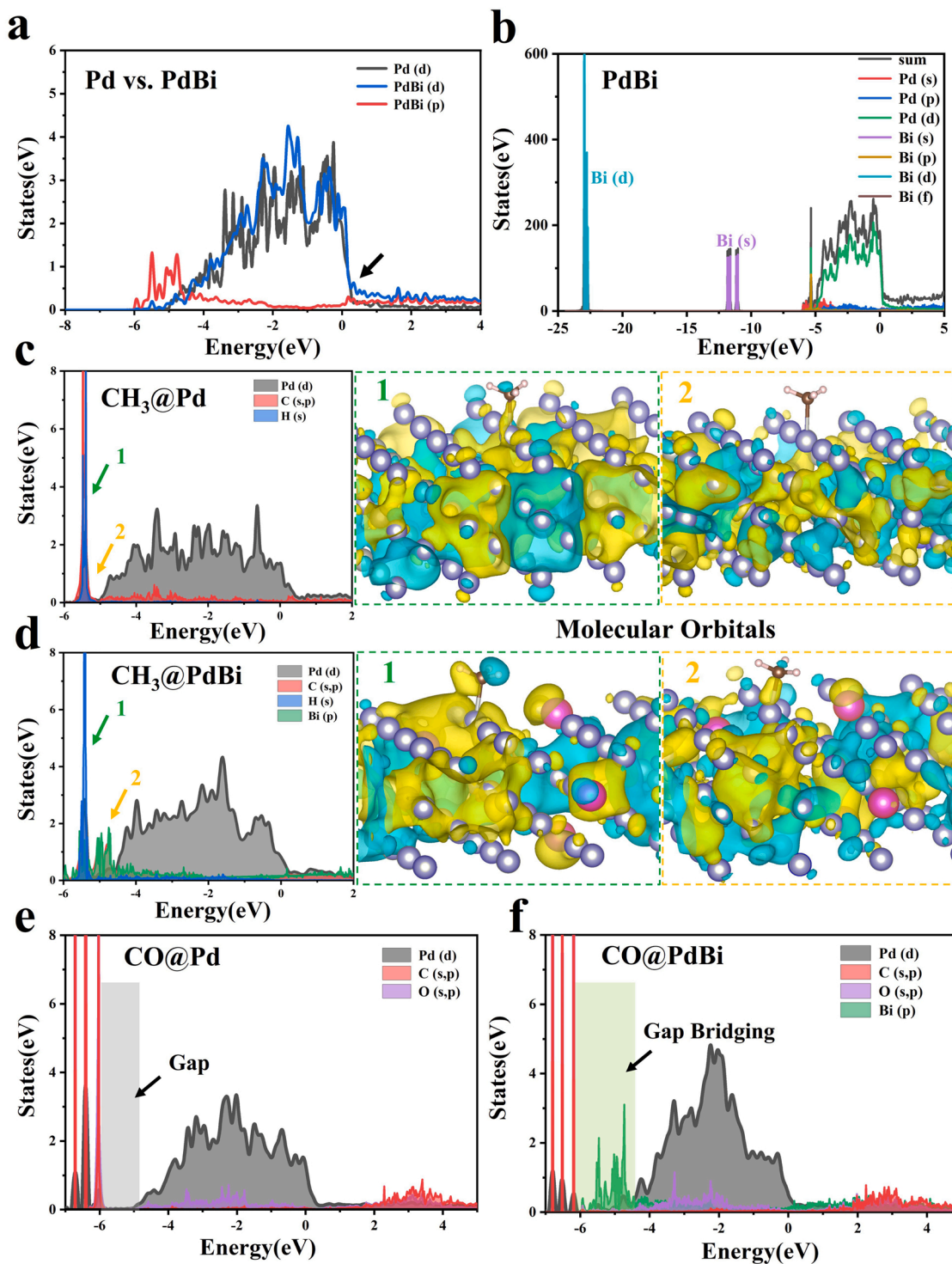

Fig. 5. The changes of PDOS and molecular orbitals (MOs) of Pd NS and PdBi NS during the progress of EOR. (a, b) PDOS of Pd NS and PdBi NS before adsorption. (c) PDOS of "CH_3 adsorbed on Pd NS" and the corresponding MOs at the energy levels of "1" and "2" in the PDOS curves. (d) PDOS of "CH_3 adsorbed on PdBi NS" and the corresponding MOs at the energy levels of "1" and "2" in the PDOS curves. (e) PDOS of "CO adsorbed on Pd NS" showing an apparent energy gap. (f) PDOS of "CO adsorbed on PdBi NS" showing the gap-bridging effect.

and blues lines in Fig. 5a), demonstrating *p-d* hybridization in the PdBi NS. However, this is not a full picture. The frontier orbitals of carbonaceous radicals should also be considered in the regulation of the band structure of PdBi NS. Since the oxidation of *CH$_3$ is the electrochemical rate-determining step in C1 pathway, we compared the change of PDOS for the structures of CH$_3$@Pd and CH$_3$@PdBi, as shown in Figs. 5c and 5d, respectively. It is well-known that *s* and *p* orbitals of C can hybridize with *s* orbitals of H, sitting at the position of "1" in Fig. 5c according to our calculations, which presents an apparent energy gap to d-band of Pd. The molecular orbital (MO) of CH$_3$@Pd at "1" also shows this *s-p* hybridization, while it disappears at "2" in Fig. 5c. Interestingly, after incorporation of Bi, the PDOS in Fig. 5d shows that *p*-orbitals of Bi not only drag down d-band of Pd, but also lifted up *s* and *p* orbitals of *CH$_3$, forming *s-p-d* hybridization that bridges the energy gap at "2". MOs of CH$_3$@PdBi at "1" and "2" can also be seen in Fig. 5d, illustrating this *s-p-d* hybridization. This observation clearly means that the oxidation of *CH$_3$ can be accelerated on PdBi due to the facilitated electron transfer from *CH$_3$ to d-band of Pd, reducing the energy barrier of the rate-determining step in C1 pathway. Moreover, the adsorbed toxic intermediate radical of *CO on PdBi (Figs. 5e and 5f) also shows the same "gap-bridging effect" and thus improves the kinetics of the oxidation of *CO to CO$_2$. The ease of eliminating *CO on PdBi correlates well with the improved anti-poisoning ability of PdBi. Similar phenomenon has also been found for CH$_3$CO@PdBi (Fig. S16), COOH@PdBi (Fig. S17), and CH$_3$@other PdBi NSs (Pd$_{39}$Bi and Pd$_{10}$Bi in Fig. S18).

It is demonstrated in this work that the change of the d-band center (Fig. S19) is not a full picture in explaining the whole EOR process. We suggest that the full picture should consider all the dynamic changes of the frontiers (the very top and bottom parts) of d-band during the progress of EOR process. More importantly, we believe that the enhanced adsorption capability before adsorption of the reactant and the *s-p-d* hybridization after adsorption of the reactant are a common mechanism for *p*-block metallic elements in improving the kinetics of all the oxidation steps in C1 pathway, which is even more pronounced for 2D ultrathin alloyed NS than that for other 3D structures.

4. Conclusion

In summary, a series of PdBi alloyed NS catalysts have been fabricated through a facile, one-pot solvothermal method. The obtained ultrathin 2D porous NS with the optimal composition of Pd$_{14.9}$Bi presented a high mass activity of 6.6 A/mg$_{pd}$ and a high specific activity of 17.9 mA/cm^2, which are 3.0 and 4.7 times higher than those of commercial Pd/C, respectively. In addition, superior anti-poisoning ability has been obtained and the selectivity of C1 pathway with 12 electrons can reach as high as 19.7 %. DFT calculations elucidated that, 1) the electron transfer from Bi to Pd enriches the surface electron density of Pd atoms for the improved adsorption capability of the CH$_3$CH$_2$OH; 2) after the adsorption of the reactant, *p*-orbitals of Bi in PdBi NS not only drag down d-band of Pd, but also lift up *s* and *p* orbitals of the adsorbed carbonaceous radicals, forming *s-p-d* hybridization that bridges the energy gap and promotes kinetics of all the oxidation steps in C1 pathway. The unconventional *s-p-d* hybridization established from the dynamic modulation of frontier orbitals of carbonaceous radicals on the band structure of PdBi NS well explains the synergistic improvement of both activity and anti-poisoning properties. This work may provide a theoretical guidance in designing highly efficient catalysts containing *p*-block metals for a broad range of applications in energy storage and conversion, including EOR, methane oxidation reactions, polysulfides reduction/oxidation reactions in lithium-sulfur batteries, anodes of sodium-ion batteries, etc.

CRediT authorship contribution statement

Liang Ji: Conceptualization, Investigation, Visualization, Writing – original draft. **Haiyun Che:** Data curation, Formal analysis. **Ningkang**

Qian: Resources, Formal analysis. **Junjie Li:** Resources, Formal analysis. **Sai Luo:** Validation, Formal analysis. **Xiao Li:** Validation, Formal analysis. **Xingqiao Wu:** Resources, Formal analysis. **Qun Xu:** Formal analysis, Writing – review & editing. **Xuzhong Gong:** Formal analysis, Writing – review & editing. **Xinwei Cui:** Supervision, Funding acquisition, Methodology, Software, Formal analysis, Writing – review & editing. **Hui Zhang:** Supervision, Project administration, Funding acquisition, Formal analysis, Methodology, Writing - review & editing. **Deren Yang:** Supervision, Writing – review & editing.

Declaration of Competing Interest

The authors declare that they have no known competing financial interests or personal relationships that could have appeared to influence the work reported in this paper.

Data Availability

Data will be made available on request.

Appendix A. Supporting information

Supplementary data associated with this article can be found in the online version at doi:10.1016/j.apcatb.2023.122521.

References

[1] M. Li, D.A. Cullen, K. Sasaki, N.S. Marinkovic, K. More, R.R. Adzic, Ternary electrocatalysts for oxidizing ethanol to carbon dioxide: making ir capable of splitting C—C bond, J. Am. Chem. Soc. 135 (2013) 132–141.

[2] C.-A. Zhou, S. Wang, K. Ma, L. Song, L. Zheng, H. Yue, Membrane-free pure H$_2$ production over single dispersed Ru-anchored Pt$_3$Ni alloys via coupling ethanol selective electrooxidation, Appl. Catal. B-Environ. 321 (2023), 122065.

[3] Z. Jiang, Q. Zhang, Z. Liang, J.G. Chen, Pt-modified TaC as an efficient electrocatalyst for ethanol oxidation in acid and alkaline electrolytes, Appl. Catal. B-Environ. 234 (2018) 329–336.

[4] Y. Zhu, L. Bu, Q. Shao, X. Huang, Subnanometer PtRh nanowire with alleviated poisoning effect and enhanced C—C bond cleavage for ethanol oxidation electrocatalysis, ACS Catal. 9 (2019) 6607–6612.

[5] S. Bai, Y. Xu, K. Cao, X. Huang, Selective ethanol oxidation reaction at the Rh-SnO$_2$ interface, Adv. Mater. 33 (2021), e2005767.

[6] M. Roca-Ayats, O. Guillén-Villafuerte, G. García, M. Soler-Vicedo, E. Pastor, M. V. Martínez-Huerta, PtSn nanoparticles supported on titanium carbonitride for the ethanol oxidation reaction, Appl. Catal. B-Environ. 237 (2018) 382–391.

[7] B. Lan, M. Huang, R.L. Wei, C.N. Wang, Q.L. Wang, Y.Y. Yang, Ethanol electrooxidation on rhodium-lead catalysts in alkaline media: high mass activity, long-term durability, and considerable CO$_2$ selectivity, Small 16 (2020), e2004380.

[8] C. Bianchini, P.K. Shen, Palladium-based electrocatalysts for alcohol oxidation in half cells and in direct alcohol fuel cells, Chem. Rev. 109 (2009) 4183–4206.

[9] Z. Chen, Y. Liu, C. Liu, J. Zhang, Y. Chen, W. Hu, Y. Deng, Engineering the metal/oxide interface of Pd nanowire@CuO$_x$ electrocatalysts for efficient alcohol oxidation reaction, Small 16 (2020), e1904964.

[10] X. Yuan, Y. Zhang, M. Cao, T. Zhou, X. Jiang, J. Chen, F. Lyu, Y. Xu, J. Luo, Q. Zhang, Y. Yin, Bi(OH)$_3$/PdBi composite nanochains as highly active and durable electrocatalysts for ethanol oxidation, Nano Lett. 19 (2019) 4752–4759.

[11] W. Huang, X.Y. Ma, H. Wang, R. Feng, J. Zhou, P.N. Duchesne, P. Zhang, F. Chen, N. Han, F. Zhao, J. Zhou, W.B. Cai, Y. Li, Promoting effect of Ni(OH)$_2$ on palladium nanocrystals leads to greatly improved operation durability for electrocatalytic ethanol oxidation in alkaline solution, Adv. Mater. 29 (2017).

[12] Y. Qin, H. Huang, W. Yu, H. Zhang, Z. Li, Z. Wang, J. Lai, L. Wang, S. Feng, Porous PdWM (M = Nb, Mo and Ta) trimetallene for high C1 selectivity in alkaline ethanol oxidation reaction, Adv. Sci. 9 (2022), e2103722.

[13] N. Ye, P. Zhao, X. Qi, W. Sheng, Z. Jiang, T. Fang, Ethanol electro-oxidation on the PdSn-TaN/C catalyst in alkaline media: making tan capable of splitting C C bond, Appl. Catal. B-Environ. 314 (2022) 121473.

[14] Z. Liang, L. Song, S. Deng, Y. Zhu, E. Stavitski, R.R. Adzic, J. Chen, J.X. Wang, Direct 12-electron oxidation of ethanol on a ternary Au(core)-PtIr(shell) electrocatalyst, J. Am. Chem. Soc. 141 (2019) 9629–9636.

[15] L. Luo, C. Fu, F. Yang, X. Li, F. Jiang, Y. Guo, F. Zhu, L. Yang, S. Shen, J. Zhang, Composition-graded Cu–Pd nanospheres with Ir-doped surfaces on n-doped porous graphene for highly efficient ethanol electro-oxidation in alkaline media, ACS Catal. 10 (2019) 1171–1184.

[16] X. Yang, Z. Liang, S. Chen, M. Ma, Q. Wang, X. Tong, Q. Zhang, J. Ye, L. Gu, N. Yang, A phosphorus-doped Ag@Pd catalyst for enhanced CC bond cleavage during ethanol electrooxidation, Small 16 (2020), e2004727.

[17] C. Shen, H. Chen, M. Qiu, Y. Shi, W. Yan, Q. Jiang, Y. Jiang, Z. Xie, Introducing oxophilic metal and interstitial hydrogen into the Pd lattice to boost electrochemical performance for alkaline ethanol oxidation, J. Mater. Chem. A 10 (2022) 1735–1741.

[18] J.K. Norskov, F. Abild-Pedersen, F. Studt, T. Bligaard, Density functional theory in surface chemistry and catalysis, PNAS 108 (2011) 937–943.

[19] J.R. Kitchin, J.K. Norskov, M.A. Barteau, J.G. Chen, Role of strain and ligand effects in the modification of the electronic and chemical properties of bimetallic surfaces, Phys. Rev. Lett. 93 (2004), 156801.

[20] M. Chu, J. Huang, J. Gong, Y. Qu, G. Chen, H. Yang, X. Wang, Q. Zhong, C. Deng, M. Cao, J. Chen, X. Yuan, Q. Zhang, Synergistic combination of Pd nanosheets and porous Bi(OH)$_3$ boosts activity and durability for ethanol oxidation reaction, Nano Res. 15 (2022) 3920–3926.

[21] B.M.Z. Wu, E. Hopkins, K. Park, Y. Chen, H. Jiang, M. Zhang, C. Zhong, L. Wang, Poisonous species in complete ethanol oxidation reaction on palladium catalysts, J. Phys. Chem. C 123 (2019) 20853–20868.

[22] F. Lyu, M. Cao, A. Mahsud, Q. Zhang, Interfacial engineering of noble metals for electrocatalytic methanol and ethanol oxidation, J. Mater. Chem. A 8 (2020) 15445–15457.

[23] J. Bai, D. Liu, J. Yang, Y. Chen, Nanocatalysts for electrocatalytic oxidation of ethanol, ChemSusChem 12 (2019) 2117–2132.

[24] Y. Qiu, J. Zhang, J. Jin, J. Sun, H. Tang, Q. Chen, Z. Zhang, W. Sun, G. Meng, Q. Xu, Y. Zhu, A. Han, L. Gu, D. Wang, Y. Li, Construction of Pd-Zn dual sites to enhance the performance for ethanol electro-oxidation reaction, Nat. Commun. 12 (2021) 5273.

[25] J. Wang, H. Ye, Y. Song, In-situ reaction-growth of PtNiX nanocrystals on supports for enhanced electrochemical catalytic oxidation of ethanol via continuous flow microfluidic process, Electrochim. Acta 278 (2018) 149–155.

[26] Q. Chen, Z. Zhou, F. Vidal-Iglesias, J. Solla-Gullon, J. Feliu, S. Sun, Significantly enhancing catalytic activity of tetrahexahedral Pt nanocrystals by Bi adatom decoration, J. Am. Chem. Soc. 133 (2011) 12930–12933.

[27] A. Dutta, R. Adhikary, P. Broekmann, J. Datta, Intelligent catalytic support by Ni/NiO/Ni(OH)$_2$ in low level of Pd/Pt boosting the performance of alkaline DEFC, Appl. Catal. B-Environ. 257 (2019), 117847.

[28] Y. Qin, M. Luo, Y. Sun, C. Li, B. Huang, Y. Yang, Y. Li, L. Wang, S. Guo, Intermetallic hcp-PtBi/fcc-Pt core/shell nanoplates enable efficient bifunctional oxygen reduction and methanol oxidation electrocatalysis, ACS Catal. 8 (2018) 5581–5590.

[29] Z. Xia, S. Guo, Strain engineering of metal-based nanomaterials for energy electrocatalysis, Chem. Soc. Rev. 48 (2019) 3265–3278.

[30] G. Kresse, J. Furthmuller, Efficient iterative schemes for ab initio total-energy calculations using a plane-wave basis set, Phys. Rev. B 54 (1996) 11169–11186.

[31] G. Kresse, J. Furthmüller, Efficiency of ab-initio total energy calculations for metals and semiconductors using a plane-wave basis set, Comput. Mater. Sci. 6 (1996) 15–50.

[32] S. Grimme, J. Antony, S. Ehrlich, H. Krieg, A consistent and accurate ab initio parametrization of density functional dispersion correction (DFT-D) for the 94 elements h-pu, J. Chem. Phys. 132 (2010), 154104.

[33] J.P. Perdew, K. Burke, M. Ernzerhof, Generalized gradient approximation made simple, Phys. Rev. Lett. 77 (1996) 3865–3868.

[34] P.E. Blochl, Projector augmented-wave method, Phys. Rev. B 50 (1994) 17953–17979.

[35] X. Yin, X. Liu, Y.T. Pan, K.A. Walsh, H. Yang, Hanoi tower-like multilayered ultrathin palladium nanosheets, Nano Lett. 14 (2014) 7188–7194.

[36] H. Yu, T. Zhou, Z. Wang, Y. Xu, X. Li, L. Wang, H. Wang, Defect-rich porous palladium metallene for enhanced alkaline oxygen reduction electrocatalysis, Angew. Chem. Ind. Ed. 133 (2021) 12134–12138.

[37] Y. Li, Y. Yan, Y. Li, H. Zhang, D. Li, D. Yang, Size-controlled synthesis of Pd nanosheets for tunable plasmonic properties, CrystEngComm 17 (2015) 1833–1838.

[38] F. Gao, Y. Zhang, F. Ren, Y. Shiraishi, Y. Du, Universal surfactant-free strategy for self-standing 3d tremella-like Pd–M (M = Ag, Pb, and Au) nanosheets for superior alcohols electrocatalysis, Adv. Funct. Mater. 30 (2020), 2000255.

[39] M. Wang, R. Ding, Y. Xiao, H. Wang, L. Wang, C.M. Chen, Y. Mu, G.P. Wu, B. Lv, CoP/rGO-Pd hybrids with heterointerfaces as highly active catalysts for ethanol electrooxidation, ACS Appl. Mater. Interfaces 12 (2020) 28903–28914.

[40] G. Bai, C. Liu, Z. Gao, B. Lu, X. Tong, X. Guo, N. Yang, Atomic carbon layers supported Pt nanoparticles for minimized CO poisoning and maximized methanol oxidation, Small 15 (2019), e1902951.

[41] B. Lan, Q.-L. Wang, Z.-X. Ma, Y.-J. Wu, X.-L. Jiang, W.-S. Jia, C.-X. Zhou, Y.-Y. Yang, Efficient electrochemical ethanol-to-CO$_2$ conversion at rhodium and bismuth hydroxide interfaces, Appl. Catal. B-Environ. 300 (2022), 120728.

[42] J. Zhang, J. Ye, Q. Fan, Y. Jiang, Y. Zhu, H. Li, Z. Cao, Q. Kuang, J. Cheng, J. Zheng, Z. Xie, Cyclic penta-twinned rhodium nanobranches as superior catalysts for ethanol electro-oxidation, J. Am. Chem. Soc. 140 (2018) 11232–11240.

[43] A. Ferre-Vilaplana, C. Buso-Rogero, J.M. Feliu, E. Herrero, Cleavage of the C—C bond in the ethanol oxidation reaction on platinum. Insight from experiments and calculations, J. Phys. Chem. C 120 (2016) 11590–11597.

[44] M. Farsadrooh, J. Torrero, L. Pascual, M.A. Peña, M. Retuerto, S. Rojas, Two-dimensional Pd-nanosheets as efficient electrocatalysts for ethanol electrooxidation. Evidences of the C C scission at low potentials, Appl. Catal. B-Environ. 237 (2018) 866–875.

[45] L.-X. Dai, X.-Y. Wang, S.-S. Yang, T. Zhang, P.-J. Ren, J.-Y. Ye, B. Nan, X.-D. Wen, Z.-Y. Zhou, R. Si, C.-H. Yan, Y.-W. Zhang, Intrinsic composition and electronic effects of multicomponent platinum nanocatalysts with high activity and selectivity for ethanol oxidation reaction, J. Mater. Chem. A 6 (2018) 11270–11280.

[46] W.D.S. Xue, F. Yang, J. Yang, I. Amiinu, D. He, H. Tang, S. Mu, Hexapod PtRuCu nanocrystalline alloy for highly efficient and stable methanol oxidation, ACS Catal. 8 (2018) 7578–7584.

[47] Y. Guo, B. Li, S. Shen, L. Luo, G. Wang, J. Zhang, Potential-dependent mechanistic study of ethanol electro-oxidation on palladium, ACS Appl. Mater. Interfaces 13 (2021) 16602–16610.